Front. Earth Sci. 2020, 14(2): 401–412
https://doi.org/10.1007/s11707-019-0779-3

RESEARCH ARTICLE

Building damage mapping based on Touzi decomposition using quad-polarimetric ALOS PALSAR data

Shan LIU[1,2,3], Fengli ZHANG (✉)[1,2,3], Shiying WEI[4], Qingbo LIU[1,2,3], Na LIU[1,2,3], Yun SHAO[1,2,3], Steven J. BURIAN[5]

1 Institute of Remote Sensing and Digital Earth Chinese Academy of Sciences, Beijing 100094, China
2 University of Chinese Academy of Sciences, Beijing 100049, China
3 Laboratory of Target Microwave Properties, Deqing Academy of Satellite Applications, Huzhou 313200, China
4 Beijing University of Civil Engineering and Architecture, Beijing 100044, China
5 Department of Civil and Environmental Engineering, University of Utah, Salt Lake City, UT 84112, USA

Abstract Building damage assessment is of great significance to disaster monitoring. Polarimetric Synthetic Aperture Radar (SAR) can record the polarization scattering measurement matrix of ground objects and obtain more abundant ground object information, meaning that they can be used for assessing damage to buildings. In this paper, a new approach is proposed to assess building damage using the Touzi incoherent decomposition and SAR-based characteristics of buildings before and after damage. The March 11th, 2011 earthquake that struck the coast of northeast Japan serves as the demonstration of the technique using quad-polarimetric ALOS PALSAR data acquired before and after the disaster. The analysis shows that after the buildings are damaged, there is a clear decrease in the α_{s1} (the dominant scattering-type magnitude) components and the degree of this reduction corresponds to the degree of building damage. This means that the α_{s1} components obtained by Touzi decomposition can effectively reflect the degree of building damage. On this basis, a model based on Touzi decomposition was established to evaluate the degree of damage to buildings, and the accuracy of the model was validated using high-resolution optical data acquired before and after the earthquake. The experimental results show that Touzi decomposition can be effectively used for damage assessment mapping in built-up areas.

Keywords Touzi decomposition, quad-polarization, SAR, buildings, damage, disaster management

Received January 12, 2019; accepted July 8, 2019

E-mail: zhangfl@aircas.ac.cn

1 Introduction

In recent years, natural disasters such as tsunamis and earthquakes have become more frequent. A timely and effective emergency response after a disaster can reduce life and economy losses. As SAR can be used in all weather conditions and at any time of day (Chen et al., 2003; Yang et al., 2010; Hao et al., 2012), it has obvious advantages for use in rescue operations and post-disaster evaluation because restrictive weather such as clouds and rain often occurs after disasters (Shen et al., 2015).

Matsuoka and Yamazaki (2000) used variations in the intensity correlation coefficient of ERS-1 data to detect damaged urban areas. Yonezawa and Takeuchi (1999) studied the interference coherence of SAR images before and after an earthquake, and found that SAR images have obvious de-coherence in damaged urban areas. This de-coherence was found to be significantly related to the amount of damage to buildings. Due to the abundant polarization information contained in quad-polarization SAR images, how to use polarization characteristics properly to extract information related to building damage has become the focus of many researchers (Zhai et al., 2016; Chen et al., 2017). Many scholars have tried to extract disaster information using data from a single date. For example, Wang et al. (2011) used a high-resolution COSMO-SkyMed image acquired after an earthquake to calculate the fractal dimension image using the triangular prism method; the results were then compared with the high-resolution optical image. The results showed that high fractal dimension values corresponded to the regions with more serious damage.

Using the circular polarization coefficient of collapsed buildings, Li proposed a method for extracting the

collapsed building area based on the polarization parameter H-$\alpha-\rho$ (Li et al., 2012). Zhai et al. (2016) used the $H/\alpha/A-$Wishart unsupervised classification method, combined with the hierarchical clustering algorithm based on the aggregation of minimum heterogeneity criteria, to extract information about earthquake damage to buildings and proved its feasibility. The polarization orientation angle (POA) compensation enhanced the polarimetric parameters and enabled extraction of collapsed buildings using the Chinese airborne SAR mapping system (SARMapper) (Zhai and Huang, 2016). They then proposed two polarimetric feature parameters for the recognition of different kinds of buildings based on entropy and eigenvalues for the Yushu earthquake (Zhai et al., 2018). In another study, Guo and colleagues (2009) used the circular polarization correlation coefficient, the even-order scattering component and anisotropy, A, to extract collapsed buildings from polarimetric SAR data acquired after the Wenchuan earthquake. Zhang et al. (2015) detected damaged buildings in RADARSAT-2 polarization data for the Yushu earthquake event by using the optimal polarization contrast enhancement method and proved that the effect was better for buildings with consistent orientation angles. However, no comparison between the situation before and after the disaster could be made using a single image and the experimental effect was not obvious.

Better information extraction can be achieved by methods that are based on using both pre-disaster and post-disaster data. The regularity of satellite orbits allows repeated visits of the same area, which produces an archive of images acquired before and after an event for comparison. Using these multi-temporal images, changes caused by disasters can be detected and understood. For example, Park detected changes between pre- and post-earthquake using ALOS PALSAR images, and found that the polarization characteristics of the post-earthquake building area, such as the $H/\alpha/A$ characteristics, the P_s, P_d, P_v scattering components, *etc.*, all changed significantly (Park et al., 2012). Chen et al. (2013 and 2016) compared several pre-disaster and post-disaster images, and found that the degree of damage to the built-up area was related to the variation in the dihedral angle scattering components and the standard deviation of the polarization azimuth angle θ. Maps of the damage were then made by using damage indicators. Thus, the use of polarization information for building damage assessment has great value and significance.

In the present study, fully polarimetric ALOS PALSAR data before and after the earthquake in north-eastern Japan that occurred on March 11th, 2011 were acquired. Touzi decomposition was performed to establish a building damage index. A building damage degree assessment model was established based on the polarization parameters. Finally, the damage mapping accuracy of the proposed method for built-up areas was validated using high resolution optical images. The remainder of the paper is divided into six main parts: experimental area and data source, experimental methods, establishment of the building damage index, mapping of building damage degree, analysis and discussion, and conclusion.

2 Experimental area and data sources

On March 11th, 2011, a magnitude 9.0 earthquake occurred off the north-east coast of Japan and seriously damaged a large number of villages and buildings (Chen and Sato, 2013). Taking the city of Ishinomaki as the experimental area, we obtained quad-polarimetric ALOS PALSAR data and GeoEye-1 optical data from before and after the disaster. Using this data we investigated the use of polarimetric SAR data to evaluate and map the damage to buildings.

The three scenes of ALOS PALSAR used in the study were acquired on April 2, 2009, November 21, 2010, and April 8, 2011 (Fig. 1). The first two scenes were before the disaster and the last scene after the disaster – all of the scenes were acquired in full polarization mode. The azimuth resolution was 4.45 m and the range resolution was 23.14 m. The specific parameters are shown in Table 1.

To obtain information about the damaged buildings, GeoEye-1 images with a resolution of 0.5 m were also obtained for time periods before and after the disaster (Figs. 2(a) and 2(b)). The images were taken on June 5, 2010 and March 19, 2011. As shown in Fig. 2, in order to investigate the scattering mechanism of buildings with different damage levels, a total of nine typical damage regions (circled in white) of four damage levels were set. The damage level values were defined as the percentage of damaged buildings in one built-up patch according to GeoEye-1 images before and after the disaster. Region 1 was the most seriously damaged with a damage level of 80%–100%; regions 7, 8, and 9 were the least damaged with damage levels of 0–20%. The damage level of the other regions was in between the two extremes, with 50%–80% in regions 2 and 3 and 20%–50% in regions 4, 5, and 6.

Table 1 Detailed parameters of the three scenes of ALOS PALSAR data

Image No.	Sensor	Acquisition date	Incidence angle/(°)	Polarization
D1	PALSAR	April 2, 2009	23.774	HH + HV + VH + VV
D2	PALSAR	November 21, 2010	23.796	HH + HV + VH + VV
D3	PALSAR	April 8, 2011	23.832	HH + HV + VH + VV

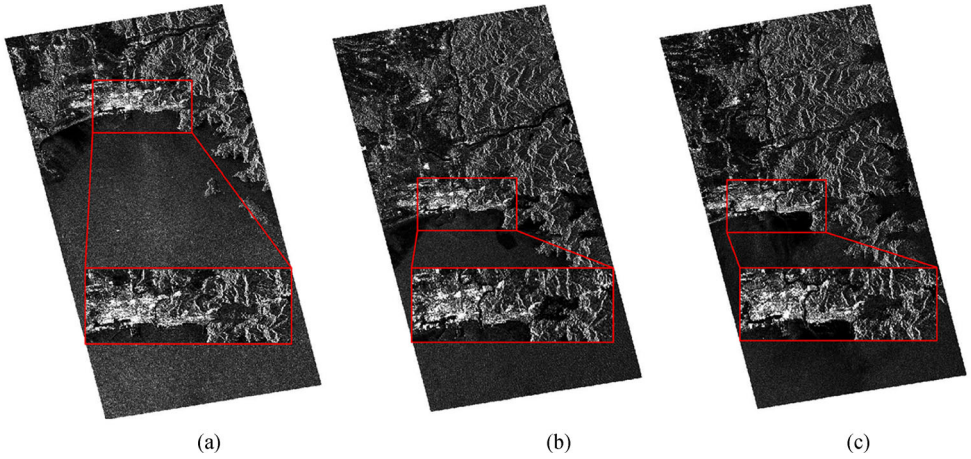

(a) (b) (c)

Fig. 1 HH polarimetric ALOS PALSAR images pre- and post-disaster. The red boxes mark the extent of experimental area for building damage mapping. (a) April 2, 2009; (b) November 21, 2009; (c) April 8, 2011.

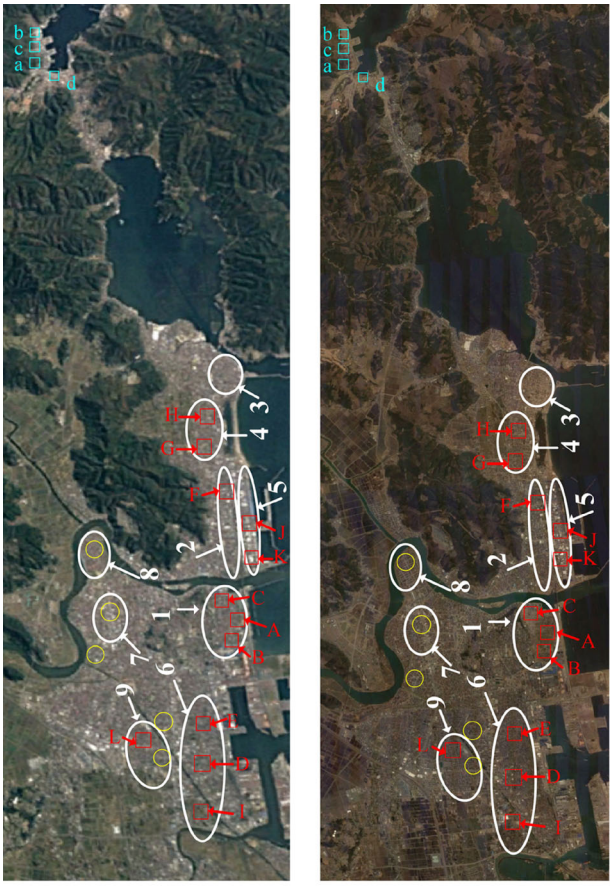

(a) (b)

Fig. 2 GeoEye-1 images with a resolution of 0.5 m before (a) and after (b) the disaster. The nine white circles numbered 1–9 represent four levels of damage, and within them there are 12 red sample areas A–L with damage degree calculated accurately. The yellow circles and blue boxes a–d show the samples used for method analyzing and validation. (a) June 5, 2010; (b) March 19, 2011.

Within these 9 regions, the damage degree values of 12 small sample areas were determined manually using high resolution GeoEye-1 images. The degree damage $DD_{\text{ground\_truth}}$ is calculated as:

$$DD_{\text{ground\_truth}} = \frac{Num_{\text{all buildings\_pre}} - Num_{\text{intact buildings\_post}}}{Num_{\text{all buildings\_pre}}} \times 100\%, \quad (1)$$

where $Num_{\text{all buildings\_pre}}$ denotes the number of buildings interpreted from the GeoEye-1 images on June 5, 2010 before the earthquake and $Num_{\text{intact buildings\_post}}$ denotes the number of intact buildings interpreted from the GeoEye-1 images on March 19, 2011. These two GeoEye-1 images were first co-registered, with the GeoEye-1 image on June 5, 2010 as the reference, then the sample areas were cropped, and the number of buildings was counted by visual interpretation. According to Eq. (1), the degree of damage $DD_{\text{ground\_truth}}$ of the 12 small sample areas (A – L) marked with red boxes in Fig. 2 was calculated as 95%, 90%, 80%, 75%, 60%, 50%, 39%, 30%, 25%, 24%, 20%, and 5% for areas A through L, respectively.

In addition, the yellow circles in Fig. 2 mark the sample buildings that did not collapse: these samples were used for analyzing and verifying the model. The samples used for mapping results validation are marked by blue boxes. The damage degree values of these sample areas were calculated using Eq. (1) to be 80%, 60%, 55%, and 35% for areas a – d, respectively.

3 Methods

For built-up areas without damage, there are mainly three kinds of scattering mechanisms (Fig. 3(a)), including

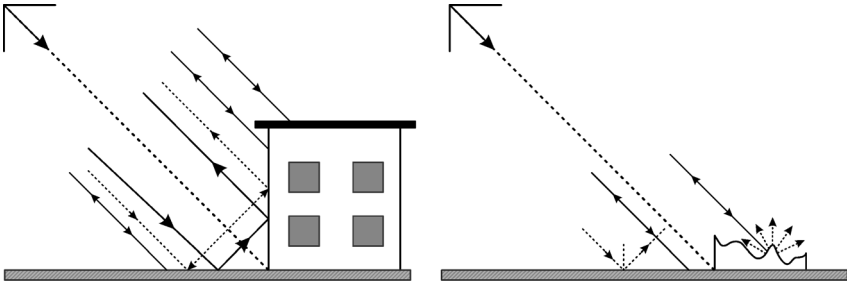

(a) Intact buildings (b) Destroyed buildings

Fig. 3 Scattering mechanisms of buildings pre- and post-disaster. (a) Intact buildings; (b) Destroyed buildings.

single-bounce scattering from ground surfaces, walls, or roofs; double-bounce scattering formed by the front wall and the ground; as well as triple-bounce scattering due to the ground-wall-ground and wall-ground-wall reflections. Of these, double bounce scattering is the most significant. However, when buildings are damaged, the scattering mechanisms would be greatly changed, as shown in Fig. 3(b). The double bounce scattering will dramatically decrease, and surface scattering will dramatically increase because the perpendicular walls collapse.

The changes of scattering mechanisms can be characterized by polarimetric SAR data, and there are many polarimetric decomposition methods for scattering mechanisms analysis. For example: Pauli decomposition, Cameron decomposition, Yamaguchi decomposition, and Touzi decomposition. In this paper, Touzi decomposition is employed in the study reported herein for scattering mechanisms analysis because it is a kind of roll-invariant incoherent decomposition method and can precisely reveal the scattering mechanism of targets. Touzi decomposition was originally developed to address the ambiguity in the Cloude – Pottier decomposition in terms of the scattering type of the specific scattering mechanism (Cloude, 1986; Touzi, 2006; Li et al., 2011). Cloude-Pottier decomposition allows the coherence matrix $[T]$ to be represented as the incoherent sum of up to three coherence matrices $[T_n]$ (Cloude, 1986; Touzi, 2006; Li et al., 2011):

$$[T] = \sum_{i=1}^{3} \lambda_i [T_i]. \tag{2}$$

Each scattering mechanism i (i = 1, 2, 3) can be represented by coherence matrices $[T_i]$ with rank 1 and corresponding to standard positive real-part eigenvalues $\lambda_i/(\lambda_1 + \lambda_2 + \lambda_3)$. The coherence matrices can be represented by target vectors $\vec{k}_i$:

$$[T_i] = \vec{k}_i \cdot \vec{k}_i^{*t}, \tag{3}$$

where * denotes the conjugate and t the transpose. Cloude pointed out that each target vector $\vec{k}_i$ has an equivalent single scattering matrix $[S]_i$ and that $\vec{k}_i$ can be expressed using the elements of this matrix (Touzi, 2006):

$$\vec{k}_i = \frac{1}{\sqrt{2}}[(S_{hh})_i + (S_{vv})_i,\ (S_{hh})_i - (S_{vv})_i,\ 2(S_{hh})_i]. \tag{4}$$

Touzi decomposition is an eigen-decomposition method based on the coherence matrix $[T]$. But, unlike Cloude-Pottier, Touzi decomposition uses a roll-invariant coherent scattering model to parameterize $\vec{k}_i$. Touzi decomposition can obtain four roll-invariant parameters (Bhattacharya and Touzi, 2012):

$$ICTD_i = (\alpha_{si},\ \phi_{\alpha si},\ \tau_i,\ \lambda_i). \tag{5}$$

Each of these coherent scattering mechanisms can be expressed in terms of α_s, $\phi_{\alpha s}$, and τ, which represent the degree of symmetry in polar coordinates. The normalized eigenvalues λ_i represent the relative energy of the scattering mechanism represented by each corresponding eigenvector i.

Touzi decomposition generates a total of 12 parameters, including the main, medium, and low scattering components (α_{si}, $\phi_{\alpha si}$, τ_i, λ_i, i = 1, 2, 3), the complex scattering type parameters α_s and $\phi_{\alpha s}$ used to provide a clear description of the scattering mechanism of symmetric targets, and τ, which represents the degree of symmetry in the target scattering. The parameter α_s characterizes the type of scattering that occurs during the interaction of the radar wave with building structures; the information provided by $\phi_{\alpha s}$ can remove scattering ambiguities; the helicity τ can identify resolution cells with mixed back-scattering from trees and buildings.

We used a 3 × 3 moving window in Touzi decomposition to calculate the values of α_{s1}, α_{s2}, α_{s3}, $\phi_{\alpha s1}$, $\phi_{\alpha s2}$, $\phi_{\alpha s3}$, τ_1, τ_2, τ_3, λ_1, λ_2, and λ_3 before and after the earthquake in nine built-up regions that had different damage levels. The results showed that there was no regularity in the changes in α_{s2}, α_{s3}, $\phi_{\alpha s1}$, $\phi_{\alpha s2}$, $\phi_{\alpha s3}$, τ_1, τ_2, τ_3, λ_1, λ_2, and λ_3 after the disaster while there was an obvious trend in the values of α_{s1}. As shown in Fig. 4, the blue line, D1, represents the

nine regions extracted from the April 2, 2009 ALOS PALSAR image; the red line, D2, represents the nine regions extracted from the November 21, 2010 ALOS PALSAR image; and the green line, D3, represents the nine regions extracted from the April 8, 2011 ALOS PALSAR image. It can be seen that, after the disaster, in these nine areas there was either a significant reduction or basically no change. Also, through the analysis of the damage levels of these areas, we found that the more serious the damage (region 1), the more the value of α_{s1} decreases. However, in regions 7, 8, and 9, where the buildings remained basically intact, the values were almost the same before and after the disaster. At the same time, the α_{s1} values of the two dates before disaster (i.e., D1 in blue and D2 in red) were also compared and analyzed. An analysis shows that the α_{s1} components of these nine regions change very little with time when there is no damage, so it can be assumed that α_{s1} is very sensitive to the damage of buildings.

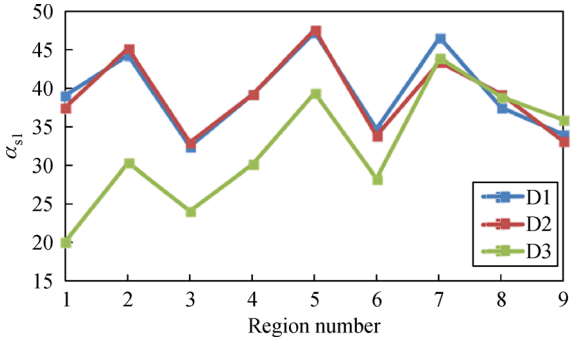

Fig. 4 Average values of α_{s1} from Touzi decomposition pre- and post-disaster for the 9 sample regions.

As previously mentioned, the value of α_{s1} represents the type of scattering mechanism generated by the interaction between the radar signal and target: $\alpha_{s1} = 0$ denotes surface scattering, $\alpha_{s1} = \frac{\pi}{4}$ denotes even-order scattering, and $\alpha_{s1} =$ 90, denotes double bounce scattering. An area of intact buildings is covered mainly by walled structures containing dihedral corners and so it corresponds mainly to double bounce scattering, giving an α_{s1} value close to $\frac{\pi}{2}$. After building collapse, however, these dihedral corners structures are destroyed and thus the double bounce scattering is reduced, causing the α_{s1} value to drop. This trend is well illustrated by Fig. 4. Therefore, we consider that the α_{s1} value derived from Touzi decomposition is an important indicator of building damage. Additionally, it is clear that by finding the difference between the values before and after the disaster, the damage degree of buildings in the area can be estimated. A diagram of the entire process is shown in Fig. 5.

As the first step, geometric correction, geocoding, registration, and multi-look processing is carried out on the ALOS PALSAR imagery. The high-resolution GeoEye-1 data was taken as the reference image and the three ALOS PALSAR images were wrapped using the cross correlation matching method, and the ultimate matching accuracy reached sub-pixel level. Second, Touzi decomposition is used to extract the α_{s1} values in the built-up area and then the ratio of the post-disaster to pre-disaster α_{s1} values is calculated. This ratio is used as a damage index to evaluate the damage degree of buildings in the affected area and establish the model for building damage degree mapping. Finally, using ground-truth data determined using high-resolution GeoEye-1 images, the accuracy of the model is evaluated.

4 Establishment of the building area damage index based on Touzi decomposition

Figure 6 shows the values of the α_{s1} in the three ALOS PALSAR images calculated by Touzi decomposition. The difference between the mountains and water for the three dates is small. In the mountainous area with vegetation, the value of α_{s1} is about 45°, and in marine and bare land, the value of α_{s1} is about 0°. In contrast, in the building area before the disaster, namely on April 2, 2009 and November 21, 2010, the value of α_{s1} is about 90° or so and the difference of these two dates is small, but after the disaster, namely on April 8, 2011, due to the damaged buildings, the value of α_{s1} is significantly reduced.

To analyze the differences of α_{s1} values of buildings with different damage levels, we selected the following regions: region 1 had the most serious damage (80%–100%); region 3 had severe damage (50%–80%); region 5 had moderate (20%–50%); and region 7 had lighter damage (0–20%). We then extracted the probability distribution functions of α_{s1} from these four areas in the three ALOS PALSAR images. Figure 7 shows the results. The distribution calculated using the ALOS PALSAR image acquired after the disaster is significantly shifted to the left with a larger peak; that is, the average value of α_{s1} decreased. The more serious the damage, the more obvious the shift of the peak to the left.

The α_{s1} distribution curves of all the pixels for the same four regions (1, 3, 5, 7) are drawn in Fig. 8 and sorted according to their values. The horizontal axis is the number of all the pixels within each region and the vertical axis represents the value of α_{s1}. Blue curves represent the image of April 2, 2009, red curves represent the image of November 21, 2010, and green curves represent the image of April 8, 2011. The trend noted in Fig. 7 is even more significant in Fig. 8. Before the damage occurred, the difference in α_{s1} due to time is small (blue line and red line). After the disaster, the value of α_{s1} in the built-up area significantly decreases (green line); also, the more serious

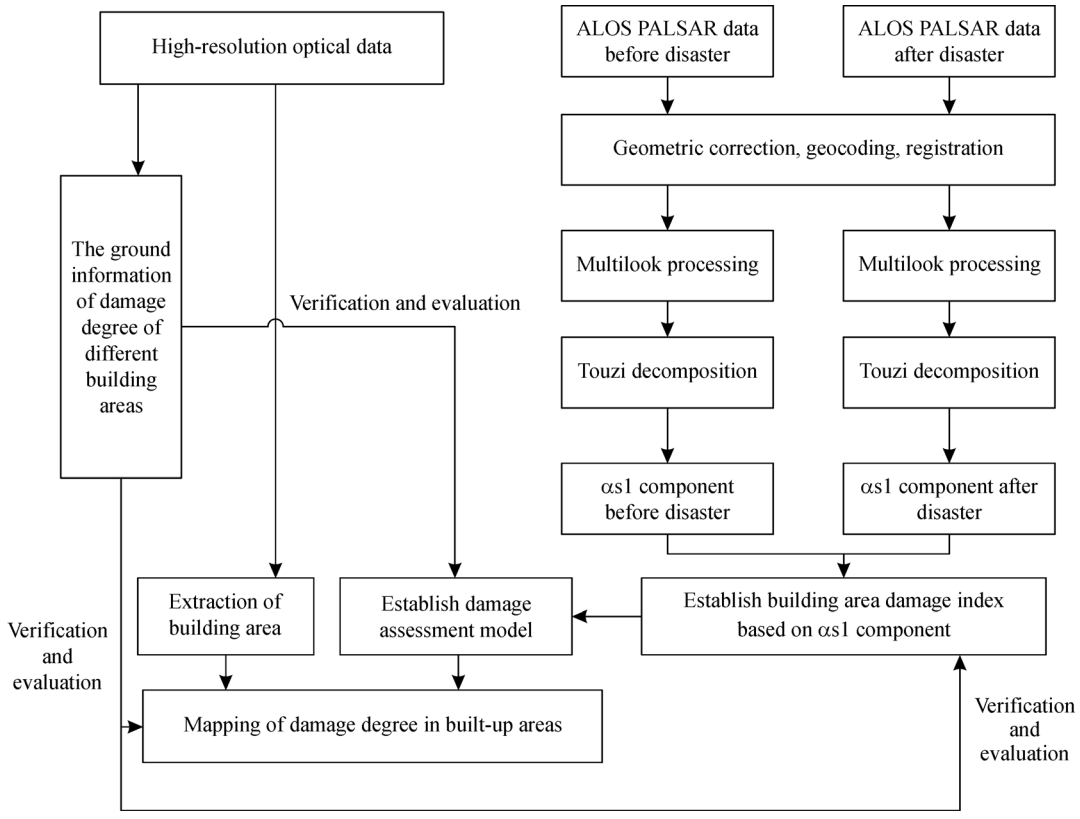

Fig. 5 Flowchart of the proposed method.

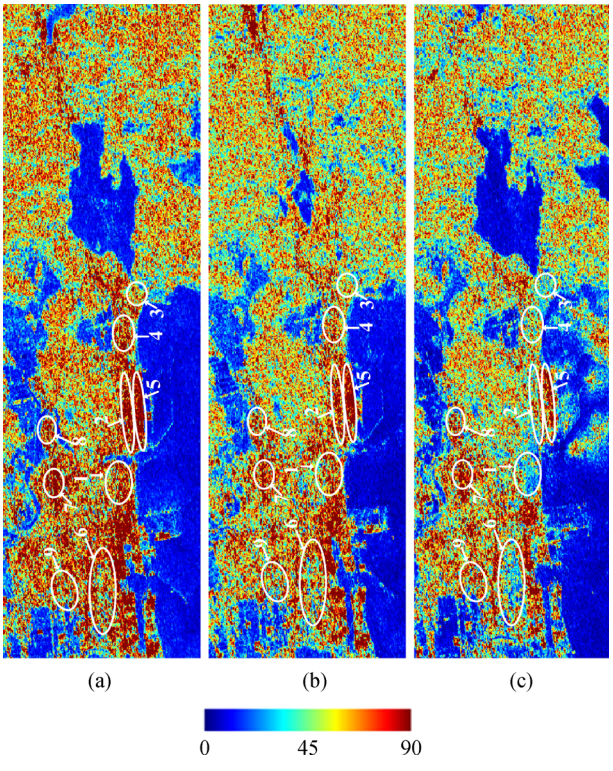

Fig. 6 α_{s1} components extracted from the three ALOS PALSAR images. (a) April 2, 2009; (b) November 21, 2010; (c) April 8, 2011.

the damage, the more obvious the reduction. From Fig. 8, the decrease in α_{s1} in region 1 > region 3 > region 5 > region 7.

To describe the degree of building damage, we define the damage index as the ratio of the post-disaster value of α_{s1} to the pre-disaster value:

$$Ratio_{\alpha_{s1}} = \frac{(\alpha_{s1})_{D_{(n,i)}}}{(\alpha_{s1})_{D_{(m,i)}}}, \quad (6)$$

where, i represents the area, and n and m, respectively, represent the acquisition date of the post-disaster and pre-disaster polarimetric SAR data.

Taking n as April 8, 2011, and m as either April 2, 2009 or November 21, 2010, the damage indexes for the nine regions described earlier can be calculated using Eq. (6), as shown in Fig. 9(a). Taking n as November 21, 2010 and m as April 2, 2009, the ratios for the two dates before the disasters in the nine regions were calculated, as shown in Fig. 9(b). In the most severely damaged region (region 1: 80%–100% damage), the ratio of post-disaster to pre-disaster α_{s1} is between 0.4 and 0.6 (Fig. 9(a)). In the severely damaged regions 2 and 3 (50%–80%), the post-disaster to pre-disaster ratio is 0.6 – 0.8. In the moderately damaged regions 4 and 6 (20%–50%), the post-disaster to pre-disaster ratio is between 0.8 and 1.0. Finally, in regions 7, 8, and 9, where the damage is lighter (0–20%), the

corresponding ratios are around 1. On the other side, Fig. 9(b) shows that the ratios of α_{s1} for the two pre-disaster dates in these nine regions with different damage levels are basically around 1. That is, for undamaged buildings, the value is relatively stable and basically does not change with time. Thus, the damage index $Ratio_{\alpha_{s1}}$ can eliminate the effect of time and guarantees the accuracy of damage evaluation.

Both the ALOS PALSAR image acquired after the disaster and the pre-disaster ALOS PALSAR image from November 21, 2010 were used to conduct the damage index calculation using the above method. First, the extent of the urban areas was extracted by referring to the high-resolution optical data and superimposed on the ALOS PALSAR image from November 21, 2010. The results are shown in Fig. 10(a). Then, a 15×15 moving window was used to calculate the damage index according to Eq. (6) after various window sizes including 3×3, 5×5, 7×7, 9×9, 15×15, and 17×17 were tried. The calculated damage index was then superimposed on the HH polarimetric ALOS PALSAR image from November 21, 2010, shown in Fig. 10(b). It can be seen that the post-disaster to pre-disaster α_{s1} ratio is between 0 and 1.5; also, the smaller the ratio, the more serious the damage. An analysis of how to use the damage index calculated using α_{s1} to map the damage degree of built-up areas follows.

5 Mapping of damage degree in built-up areas

From the analysis described above, the damage index $Ratio_{\alpha_{s1}}$ was obtained. According to the analysis shown in Fig. 9, there is an inverse correlation between the damage index calculated by Eq. (6) and the damage levels in built-up areas. That is, the smaller the ratio between the post-disaster and pre-disaster α_{s1}, the greater the damage. This quantitative relationship between $Ratio_{\alpha_{s1}}$ and damage degree is further analyzed using the 12 sample areas (A – L marked as red boxes in Fig. 2) set within the nine regions of various damage levels.

According to Eq. (1), the damage degrees of sample area A–L were calculated as 95%, 90%, 80%, 75%, 60%, 50%, 39%, 30%, 25%, 24%, 20%, and 5% respectively, which was consistent with the ground survey results obtained by ZENRIN Japan (Chen and Sato, 2013). The GeoEye-1 images for sample area A-H before and after the earthquake are respectively shown in Fig. 11.

Then the damage index $\text{Ratio}_{\alpha_{s1}}$ was extracted from Fig. 10(b) and the calculated ground-truth damage degrees for these 12 regions were combined to produce a scatter diagram; the results are shown in Fig. 12. The primary observation from this figure is an inverse correlation between the damage degree and the damage index. A linear relationship can be used to match them. Most of the points are evenly distributed along the trend line or on both sides of the trend line and so we suggest using a linear model to express the relationship between the damage degree and the damage index:

$$DD = k \cdot Ratio_{\alpha_{s1}} + b \quad 0 \leqslant Ratio_{\alpha_{s1}} \leqslant 1.5, \tag{7}$$

where k and b represent two parameters to be determined, and k is less than 0. The relationship between the damage degree $DD_{\text{ground\_truth}}$ and damage index value $Ratio_{\alpha_{s1}}$ established by using these 12 samples is shown in Fig. 12, where, $k = -2.0138$ and $b = 1.948$. The *RMSE* (root mean square error) of the fitting model was calculated as 0.0726.

6 Analysis and discussion

Due to the fluctuation of the backscattered radar echoes caused by time variations and surrounding ground targets, the value of $Ratio_{\alpha_{s1}}$ may be over 1. Therefore, five sample areas that did not experience building collapse (marked as yellow circles in Fig. 2) were selected for analysis; the calculated values of $Ratio_{\alpha_{s1}}$ of the five areas are shown in Fig. 13. We observe that the values of $Ratio_{\alpha_{s1}}$ for the five sample areas that did not collapse are between 0.9 and 1.2; that is, if the damage index value $Ratio_{\alpha_{s1}}$ exceeds 0.9, it can be assumed that the degree of damage indicated by the damage index is inaccurate and the building may not have been damaged at all. Therefore, the scope of Eq. (7) should be limited to the range $[0,\ 0.9]$. In terms of this study, when the damage degree was less than 20%, the model could mistakenly suggest that buildings without damage had been damaged. Therefore, we only considered a damage degree of about 20% to 100% when using the above model for damage mapping.

Finally, the damage degree map of the test area calculated using Eq. (7) is shown in Fig. 14. Areas with a damage degree of less than 20% are not included on the map. Comparing the nine regions shown in Fig. 2, it is clear that the damage degrees calculated using the method presented in this paper are consistent with the actual damage degrees of the nine regions. On the map, region 1 is shown in red whereas the actual damage degree was 80% – 100%; regions 2 and 3 are in orange and yellow, corresponding to actual damage degrees of 50% – 80%; regions 4, 5, and 6 are shown in cyan, corresponding to actual damage degrees of 20% – 50%; regions 7, 8, and 9 with damage degrees of 0–20% are not displayed. The damage degrees of these nine regions, as shown in the damage map obtained in this study, lie within the appropriate ranges, which is consistent with the results obtained by ZENRIN Japan (Chen and Sato, 2013).

To further validate the accuracy of the method, 4 sample areas, a–d, (marked as blue boxes in Fig. 2) in Onagawa-cho that were far away from the nine regions were taken as validation samples. Details of the calculated damage

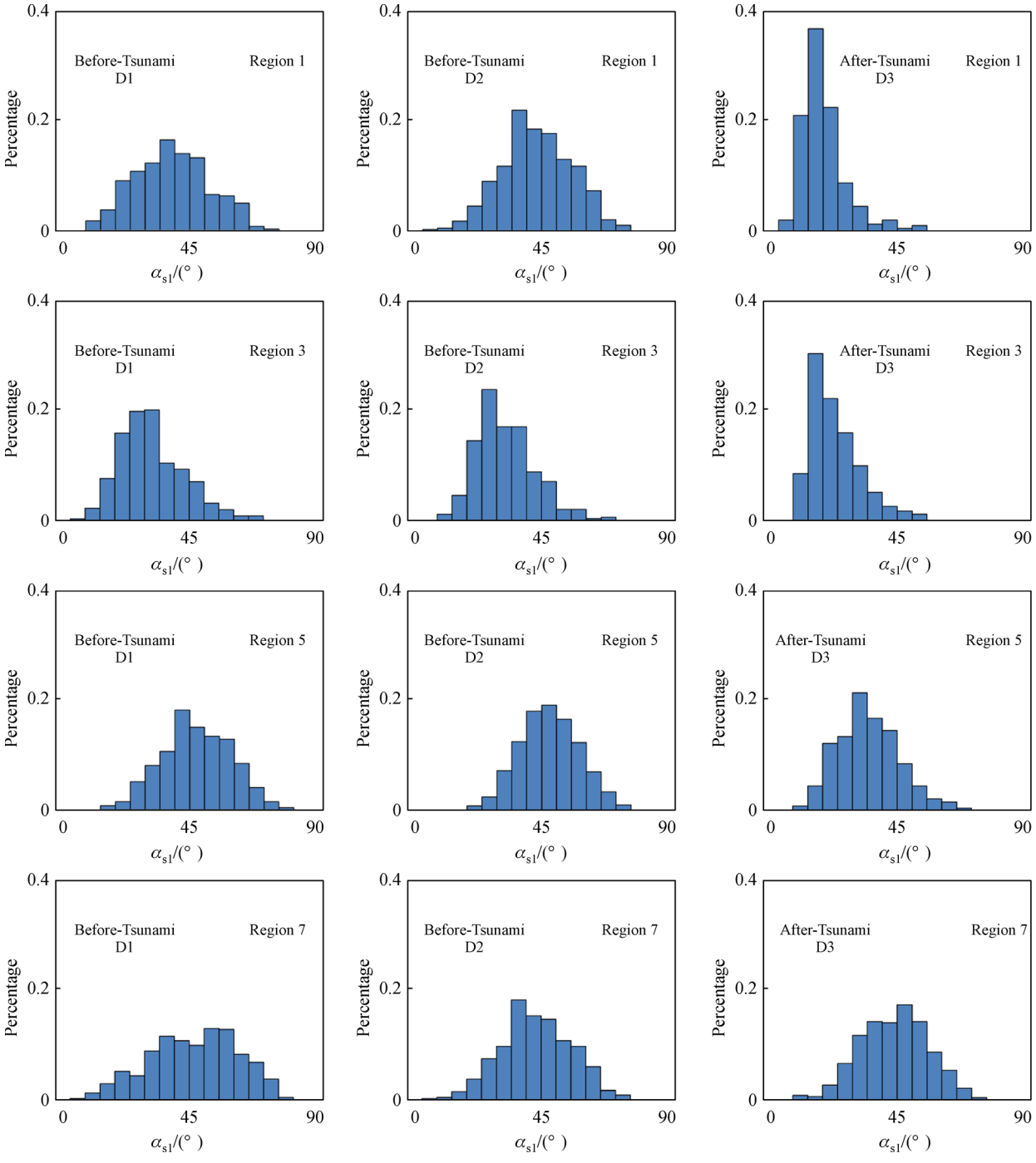

Fig. 7 Probability distributions of α_{s1} values for buildings with different damage levels extracted from ALOS PALSAR images of the three dates.

degree of this region are shown in the right of Fig. 14. The high resolution GeoEye-1 images of the four sample areas before and after the earthquake are shown in Fig. 15, and the ground-truth damage degrees calculated according to Eq. (1) are 80%, 60%, 55%, and 35%, respectively. Then the damage degrees calculated by the model described in Eq. (7) were compared with the ground-truth results. The *RMSE* for this comparison was 0.12, showing that the model has a high degree of accuracy. Further details are shown in Table 2.

Then comparisons were made between the proposed method and works of Chen et al. (2016), who performed damage mapping based on Yamaguchi decomposition. They used a double-bounce scattering component, a volume-bounce scattering component, and an odd-bounce scattering component to establish the damage index and

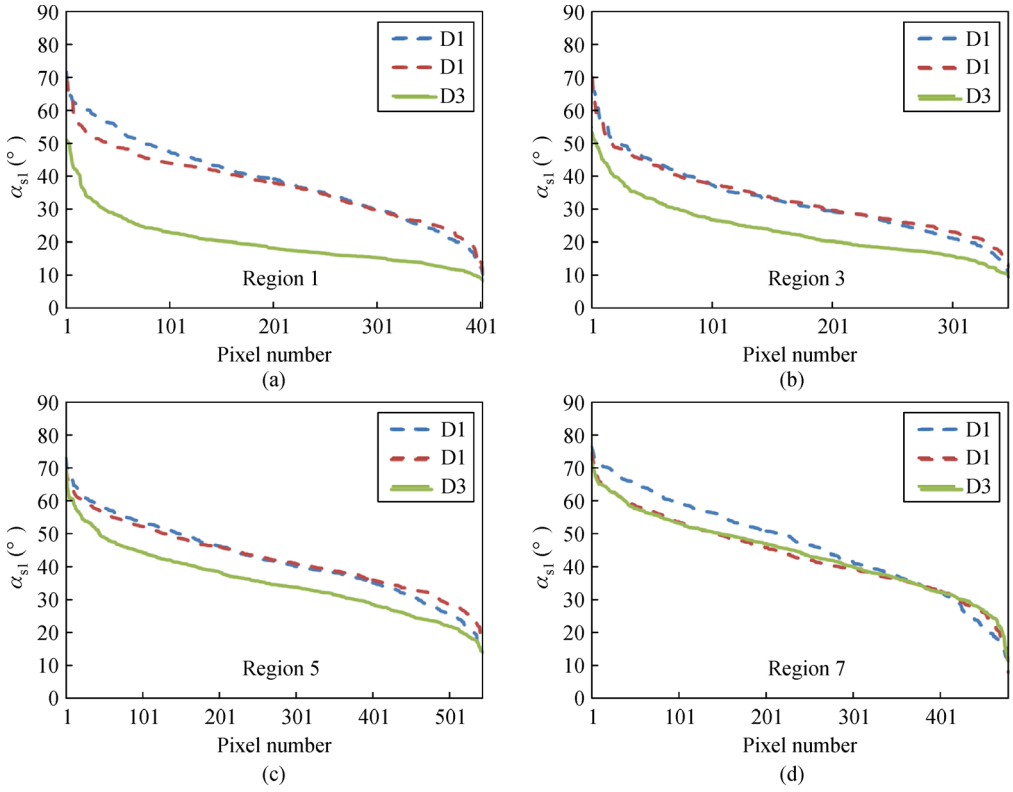

Fig. 8 The distribution curve of α_{s1} values after sorting for buildings with different damage levels extracted from ALOS PALSAR images of the three dates.

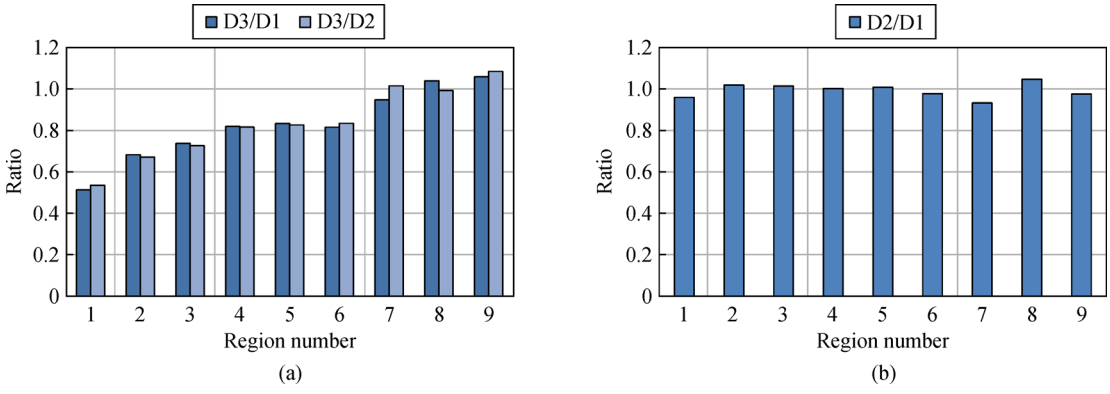

Fig. 9 Damage indexes for the 9 regions obtained using three ALOS PALSAR images. (a) Two dates before and after disaster; (b) Two dates before disaster.

map damage degree. Comparison experiments show that our method has similar accuracy to Chen's method, while our method possesses higher computation efficiency because our model is based on a sole polarimetric parameter α_{s1} derived from Touzi decomposition. In contrast, Chen's method uses three polarimetric parameters after Yamaguchi decomposition, and then calculates the percentage of dominant scattering. With the computer configuration of the Intel (R) Core (TM) i7-3770 CPU, 3.40 GHz, 4.00 GB of memory, and Windows 10 operating system, our method needs 26 min to accomplish damage mapping for the whole scene of the ALOS PALSAR image. Chen's method, however, needs 41 min, which means the computation efficiency of our proposed method is 1.5 times more efficient than Chen's method.

7 Conclusions

In this paper, the α_{s1} components calculated by Touzi decomposition were used to characterize the damage degree of built-up areas, and an evaluation model was established. The approach is based on the idea that double bounce scattering will decrease after damage to buildings

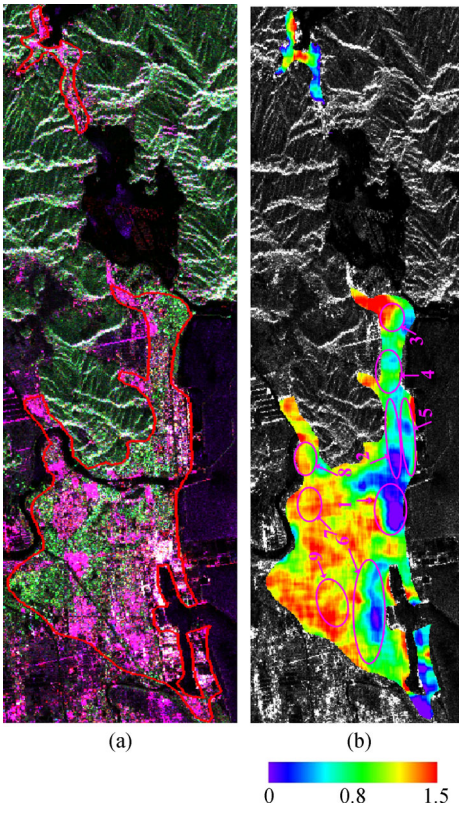

Fig. 10 (a) Extracted urban areas superimposed on the ALOS PALSAR image from November 21, 2010 (R: HH, G: HV, B: VV); (b) Damage index map of built-up areas superimposed on the HH polarimetric ALOS PALSAR image from November 21, 2010.

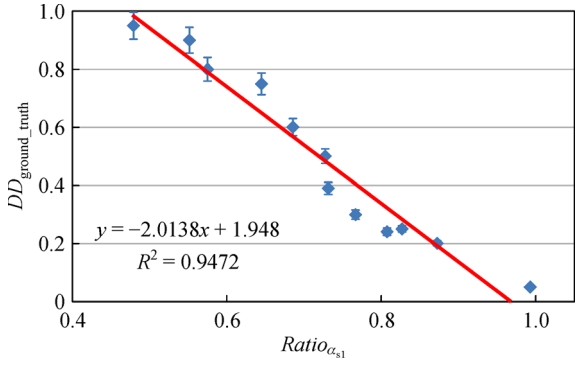

Fig. 12 Relationship between the damage degree DD_{ground_truth} and the damage index $Ratio_{\alpha_{s1}}$.

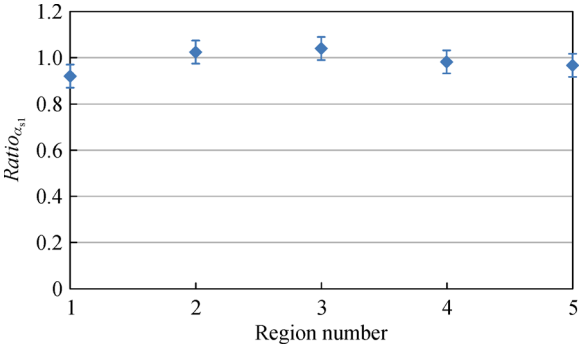

Fig. 13 The damage index of the five sample areas that did not experience building collapse.

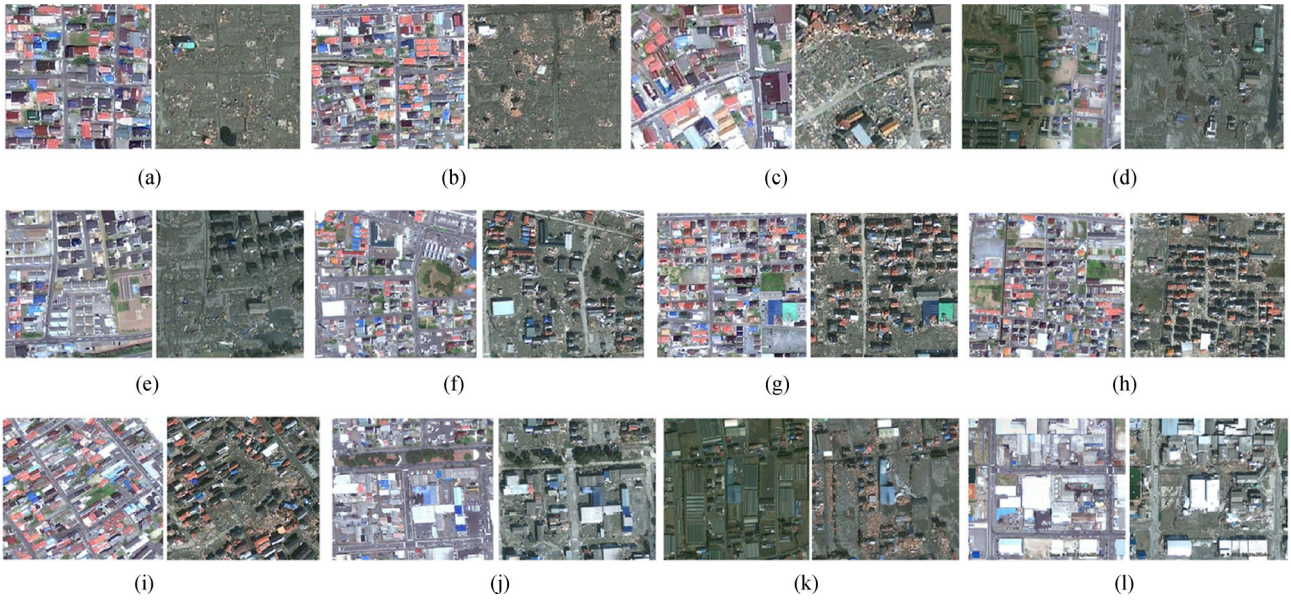

Fig. 11 The GeoEye-1 images for the 12 sample areas (A–L) acquired on June 5, 2010 and March 19, 2011. (a) Sample area A; (b) Sample area B; (c) Sample area C; (d) Sample area D; (e) Sample area E; (f) Sample area F; (g) Sample area G; (h) Sample area H; (i) Sample area I; (j) Sample area J; (k) Sample area K; (l) Sample area L.

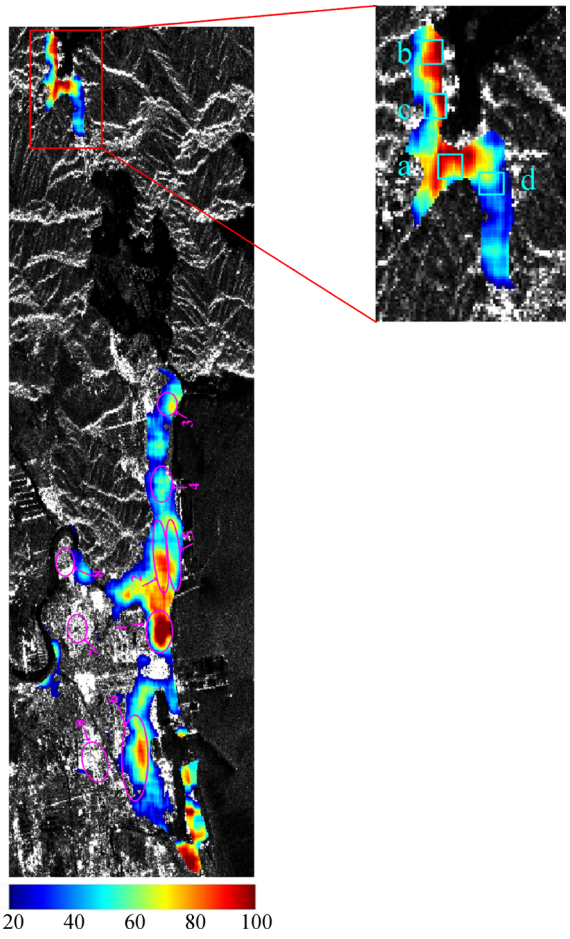

Fig. 14 The calculated damage degree map and detailed map for verification sample areas.

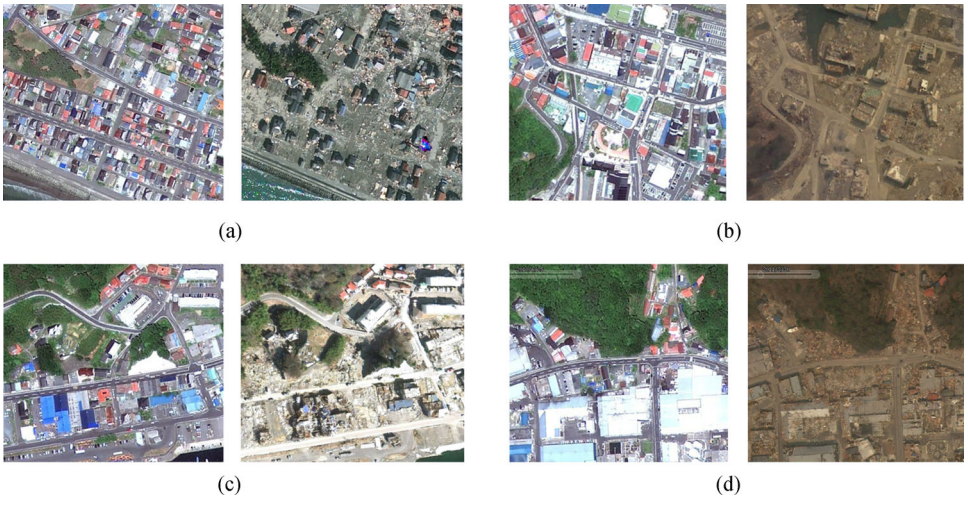

Fig. 15 The GeoEye-1 images for the four validation sample areas (a–d) acquired on June 5, 2010 and March 19, 2011. (a) Sample area A; (b) Sample area B; (c) Sample area C; (d) Sample area D.

Table 2 Error evaluation of damage degree mapping

Sample area	Truth-value	Measured value	*RMSE*
a	0.80	0.58	0.12
b	0.60	0.55	
c	0.55	0.48	
d	0.35	0.30	

has occurred. Three quad-polarized ALOS PALSAR images acquired before and after the earthquake that occurred in Japan in March 2011 were used for testing and analysis. The results showed that the α_{s1} component of the Touzi decomposition is sensitive to the building damage and that the ratio of the post-disaster to pre-disaster α_{s1} values can efficiently measure the damage degree of buildings. The established model for damage degree mapping shows high accuracy and high computation efficiency. At present, the main problem with this model is that it is not accurate for regions with lower degrees of damage and so it is only applicable for mapping in regions where the damage degree is more than 20%. In addition, we are aiming to seek more polarimetric SAR data to assess the feasibility of the proposed method, though it seems difficult currently. The prerequisite of simultaneous acquisition of pre- and post-disaster polarimetric SAR data will restrict the application of the proposed method in emergency cases, which is anticipated to be overcome in the near future by the launch of several polarimetric SAR satellites in the aid of Spatial Infrastructure Planning of China.

Acknowledgements This research was jointly supported by the National Key Research and Development Program of China (Nos. 2016YFB0502504 and 2016YFB0502500), the National Natural Science Foundation of China (Grant Nos. 41671359 and 61471358), the ALOS Research Program (No. PI1404), and the TanDEM Research Program (No. OTHER6984). In addition, the authors would like to thank the anonymous reviewers for their constructive comments and suggestions.

References

Bhattacharya A, Touzi R (2012). Polarimetric SAR urban classification using the Touzi target scattering decomposition. Can J Rem Sens, 37 (4): 323–332

Chen L Z, Shen X H, Tian Q J (2003). SAR technique and its application to geologic and seismic research. Earthquake, 23: 30–36 (in Chinese)

Chen Q H, Nie Y L, Li L L, Liu X G (2017). Buildings damage assessment using texture features of polarization decomposition components. J Remot Sens, 21: 955–965

Chen S W, Sato M (2013). Tsunami damage investigation of built-up areas using multitemporal spaceborne full polarimetric SAR images. IEEE Trans Geosci Remote Sens, 51(4): 1985–1997

Chen S W, Wang X S, Sato M (2016). Urban damage level mapping based on scattering mechanism investigation using fully polarimetric SAR data for the 3.11 east Japan earthquake. IEEE Trans Geosci Remote Sens, 54(12): 6919–6929

Cloude S R (1986). Group theory and polarisation algebra. Optik (Stuttg), 75: 26–36

Guo H D, Li X W, Zhang L (2009). Study of detecting method with advanced airborne and spaceborne synthetic aperture radar data for collapsed urban buildings from the Wenchuan earthquake. J Appl Remote Sens, 3(1): 131–136

Hao H M, Zhang Y H, Shi H Y (2012). Application of test statistic method in fully polarimtric SAR change detection. Yaogan Xuebao, 16: 520–532

Li K, Shao Y, Touzi R, Brisco B, Zhang F L (2011). Rice monitoring using touzi decomposition based on polarimetric SAR data in southwestern China. In: Proceedings of Progress in Electromagnetics Research Symposium. Suzhou: 827–830

Li X W, Guo H D, Zhang L, Chen X, Liang L (2012). A new approach to collapsed building extraction using RADARSAT-2 polarimetric SAR imagery. IEEE Geosci Remote Sens Lett, 9(4): 677–681

Matsuoka M, Yamazaki F (2000). Characteristics of satellite SAR images in the areas damaged by earthquakes. In: Blanchard A, Goodenough D, eds. Geoscience and Remote Sensing. Honolulu: IEEE, 2693–2696

Park S E, Yamaguchi Y, Singh G, Kobayashi H (2012). Polarimetric SAR remote sensing of earthquake/tsunami disaster. In: Moreira A, Desnos L, eds. Geoscience and Remote Sensing. Munich: IEEE, 1170–1173

Shen J C, Xu X, Dong H, Gui R, Song C (2015). Collapsed building extraction from single full polarimetric SAR image after earthquake. Sci Technology Eng, 15: 86–91 (in Chinsese)

Touzi R (2006). Target scattering decomposition in terms of roll-invariant target parameters. IEEE Trans Geosci Remote Sens, 45(1): 73–84

Wang X Q, Jin D J, Dou A (2011). Study on the fractal analysis of SAR images and its application to the extraction of seismic damage of 2010 Yushu, China Ms = 7.1 earthquake. In: Sato M, eds. Geoscience and Remote Sensing. Vancouver: IEEE, 1981–1984

Yang T, Gong H L, Li X J, Zhao W J (2010). Application of SAR to remote sensing of geological disasters. J Nat Disaster, 19(5): 42–48

Yonezawa C, Takeuchi S (1999). Detection of urban damage using interferometric SAR decorrelation. In: Alpers W, eds. Geoscience and Remote Sensing. Hamburg: IEEE, 925–927

Zhai W, Huang C L (2016). Fast building damage mapping using a single post-earthquake PolSAR image: a case study of the 2010 Yushu earthquake. Earth Planets Space, 68(1): 1–12

Zhai W, Huang C L, Pei W S (2018). Two new polarimetric feature parameters for the recognition of the different kinds of buildings in earthquake-stricken areas based on entropy and eigenvalues of PolSAR decomposition. Remote Sensing, 10.10: 1613

Zhai W, Shen H F, Huang C L, Pei W S (2016). Building earthquake damage information extraction from a single post-earthquake PolSAR image. Remote Sens, 8(3): 171

Zhang H Z, Wang Q, Zeng Q M, Jiao J (2015). A novel approach to building collapse detection from post-seismic polarimetric SAR imagery by using optimization of polarimetric contrast enhancement. In: Pascazio V, B. Serpico S, eds. Geoscience and Remote Sensing. Milan: IEEE, 3270–3273